Modeling and design of planar slanted volume holographic gratings for wavelength-division-multiplexing applications

Jian Liu, Ray T. Chen, Brian M. Davies, and Lifeng Li

Holographic gratings are modeled and designed for path-reversed substrate-guided-wave wavelength-division demultiplexing (WDDM) as a continuation of earlier research [Appl. Opt. **38,** 3046 (1999)]. An efficient and practical method is developed to simulate the slanted volume holographic gratings. The trade-off between dispersion and the bandwidth of the holograms is analyzed. A 60° (incident angle of the grating)/60° (diffraction angle of the grating in air) grating structure is selected to demultiplex optical signals in the 1555-nm spectral region, and a 45°/45° grating structure is chosen for the spectral region near 800 nm. Experimental results are consistent with the simulation results for these two WDDM devices. A four-channel WDDM is also demonstrated at a center wavelength of 1555 nm and with a channel spacing of 2 nm. © 1999 Optical Society of America

OCIS codes: 050.7330, 050.1960, 060.4230, 060.2340, 200.4650, 060.1810.

1. Introduction

For previous substrate-guided-wave holograms for wavelength division demultiplexing (WDDM),[1,2] optical signals of various wavelengths were dispersed by an input holographic grating, propagated within a waveguiding plate with total internal reflection, and then coupled out of the substrate by output holographic gratings. The interchannel wavelength separation of such a WDDM is totally dependent on the length between the input and the output couplers. To obtain a smaller channel wavelength spacing such as 0.8 nm requires use of a long substrate. Meanwhile, a lens array is always needed to couple the output optical signals with different wavelengths into a fiber array. Recently, path-reversed substrate-guided-wave optical interconnects for dense WDDM were proposed,[3] as shown in Fig. 1. In this approach, the beveled edge provides a way to overcome the limitation of the critical angle of the waveguiding substrate and to enhance the dispersion of the holographic grating. The grating is a path-reversed structure because the optical signals are dispersed by the output waveguide hologram for which the input light comes from the waveguiding plate and the diffracted light goes into the air. Only one lens is needed to couple the dispersed optical signals into their designated fibers. Moreover, multiple fan-outs can be realized by integration of a cascaded holographic grating array on the same waveguiding plate.[3]

In the research reported in Ref. 3, two of the present authors investigated design issues of volume holographic gratings for WDDM in terms of dispersion and bandwidth and demonstrated experimental results near 800-nm wavelength; a theoretical interpretation of the experimental results of the diffraction efficiency was not given there. As the optical signals go from larger to lower refractive-index media, backward diffraction is encountered.[3,4] Rigorous coupled-wave analysis (RCWA) has proved to be a powerful tool to simulate diffraction efficiency of gratings. In this paper we develop an efficient and practical method to solve the complicated linear equations and to overcome the instability problem for thick gratings.[5,6] Experiments were carried out to verify the validity of our theoretical simulations at center wavelengths of 1555 nm and 800 nm.

When this research was performed, J. Liu and R. T. Chen were with the Microelectronics Research Center, Department of Electrical and Computer Engineering, University of Texas at Austin, Austin, Texas 78758. J. Liu is now with Lucent Technologies, Specialty Fiber Devices, 25 Schoolhouse Road, Somerset, New Jersey 08873. B. M. Davies is with Radiant Research, Inc., 3006 Longhorn Boulevard, Austin, Texas 78758. L. Li is with the Optical Sciences Center, University of Arizona, Tucson, Arizona 85721. R. T. Chen's e-mail address is raychen@uts.cc.utexas.edu.

Received 7 May 1999; revised manuscript received 19 August 1999.

0003-6935/99/346981-06$15.00/0

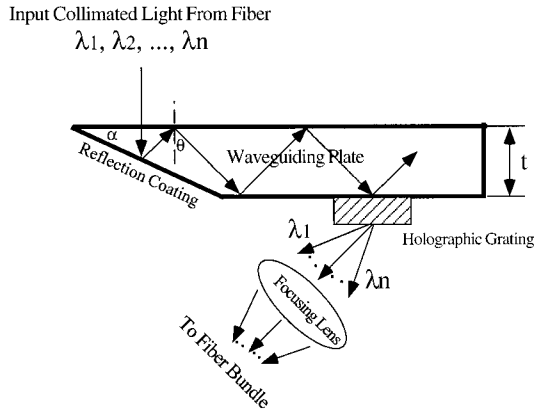

Fig. 1. Configuration of a path-reversed substrate-guided wave holographic grating.

In Section 2 we develop a form of RCWA that is specific to the case of a slanted volume grating surrounded by slabs of dielectric. In implementing the resulting method we use a program (written in Matlab in our case) to calculate the quantities of interest in our WDDM device. Section 3 presents simulation results, followed by presentation of experimental results in Section 4. Section 5 summarizes our results.

2. Modeling of Planar Slanted Volume Gratings

As shown in Fig. 2(a), the space of the volume holographic grating is divided into three regions, the superstrate, the grating layer, and the substrate, labeled $+1$, 0, and -1, respectively. All media are assumed isotropic and nonmagnetic ($\mu = 1$). The permittivities $\varepsilon^{(\pm 1)}$ are constants. Because the incident plane wave is assumed to be in the superstrate, $\varepsilon^{(+1)}$ must be real. The time dependence $\exp(-i\omega t)$ is used. So the imaginary part of the other two permittivities must be positive. The thickness of region 0 is d, and angle ζ, $|\zeta| < \pi/2$, formed between the fringe plane and the grating normal is called the slant angle.

Figure 2(b) shows three coordinate systems that are all natural to the grating problem. System xOy is good for describing the overall grating geometry. System XOY is natural to the grating fringes. Oblique Cartesian system x_1Ox_2 is our working coordinate system. It is natural to both the overall grating problem and the periodic fringes, making the mathematical analysis easy. Note that this RCWA approach is different from that of Gaylord and Moharam[4] because we use a more convenient coordinate system.

The transformations between these systems are

$$x_1 = x - y \tan \zeta = X/\cos \zeta,$$
$$x_2 = y/\cos \zeta = Y - X \tan \zeta. \tag{1}$$

In all cases, the third coordinate axis $z = Z = x_3$ is perpendicular to the other two axes. The permittivity is invariant along the z axis. In system XOY the

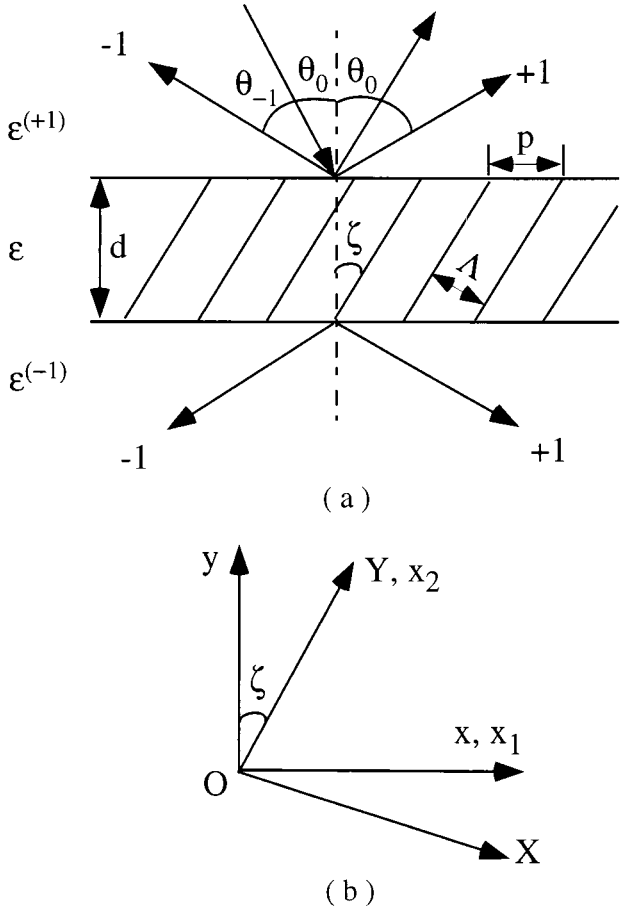

Fig. 2. Grating structure and coordinate systems used for RCWA.

permittivity function is given by $\varepsilon(X) = \varepsilon(X + \Lambda)$, where Λ is the fringe period. However, for the overall grating structure, the period is $p = \Lambda/\cos\zeta$. In system x_1Ox_2, the permittivity function is $\varepsilon(x_1) = \varepsilon(x_1 + p)$, $\partial\varepsilon/\partial x_2 = 0$. It is assumed that the derivatives of $\varepsilon(x_1)$ up to at least the second order are continuous. This means that surface-relief gratings are excluded from this study.

The direction of the incident plane wave, specified by angle θ_0, is in the xOy plane (nonconical incidence case). Its polarization can be TE or TM (with the electric or magnetic vector along the z axis). Random polarization can be treated as a power superposition of the two fundamental polarizations.

In coordinate system $Ox_1x_2x_3$, for the nonconical diffraction case, Maxwell's equations reduce to the following two uncoupled sets of equations:

$$\partial_2 E_3 = i \frac{k_0\mu}{\cos \zeta} (H_1 - \sin \zeta H_2),$$
$$-\partial_1 E_3 = i \frac{k_0\mu}{\cos \zeta} (H_2 - \sin \zeta H_1),$$
$$\partial_1 H_2 - \partial_2 H_1 = -ik_0\varepsilon \cos \zeta E_3 \tag{2a}$$

in TE polarization and

$$\partial_2 H_3 = -i\,\frac{k_0\varepsilon}{\cos\zeta}\,(E_1 - \sin\zeta E_2),$$

$$-\partial_1 H_3 = -i\,\frac{k_0\varepsilon}{\cos\zeta}\,(E_2 - \sin\zeta E_1),$$

$$\partial_1 E_2 - \partial_2 E_1 = ik_0\mu\cos\zeta H_3 \tag{2b}$$

in TM polarization. In Eqs. (2), E_l and H_l are the (covariant) field components along axis x_l, $l = 1, 2, 3$, and $k_0 = 2\pi/\lambda$ is the vacuum wave number. In the equation numbers for Eqs. (2), a means TE polarization and b means TM polarization. This method of numbering the equations is used in the rest of this section. Equations that are valid for both polarizations are not so labeled.

From Eqs. (2) it follows that

$$\frac{\partial_2}{i}\begin{pmatrix}E_3\\H_1\end{pmatrix} = \begin{bmatrix}\sin\zeta\,\dfrac{\partial_1}{i} & k_0\mu\cos\zeta\\ \dfrac{\cos\zeta}{k_0\mu}\left[k_0^2\varepsilon\mu - \left(\dfrac{\partial_1}{i}\right)^2\right] & \sin\zeta\,\dfrac{\partial_1}{i}\end{bmatrix}\begin{pmatrix}E_3\\H_1\end{pmatrix}, \tag{3a}$$

$$\frac{\partial_2}{i}\begin{pmatrix}H_3\\E_1\end{pmatrix} = \begin{pmatrix}\sin\zeta\,\dfrac{\partial_1}{i} & -k_0\varepsilon\cos\zeta\\ -\dfrac{\cos\zeta}{k_0}\left(k_0^2\mu - \dfrac{\partial_1}{i}\dfrac{1}{\varepsilon}\dfrac{\partial_1}{i}\right) & \sin\zeta\,\dfrac{\partial_1}{i}\end{pmatrix}\begin{pmatrix}H_3\\E_1\end{pmatrix}. \tag{3b}$$

In region ± 1 the solutions of Eqs. (3a) and (3b) can be written as Rayleigh expansions. In medium $+1$ we have

$$F_3(x_1, x_2) = \exp[i\alpha_0 x_1 + i\beta_0^{(+1)-}x_2] + \sum_n R_n \exp[i\alpha_n x_1 + i\beta_n^{(+1)+}x_2], \tag{4}$$

where F_3 stands for E_3 or H_3; R_n, $n = \ldots, -1, 0, +1, \ldots$, are the reflected diffraction amplitudes. The first term in Eq. (4) represents the incident plane wave, whose amplitude has been set to unity. In medium -1 the Rayleigh expansion is

$$F_3(x_1, x_2) = \sum_n T_n \exp[i\alpha_n x_1 + i\beta_n^{(-1)-}x_2], \tag{5}$$

where T_n are the transmitted diffraction amplitudes. In Eqs. (4) and (5) the α and β coefficients are given by

$$\alpha_n = \alpha_0 + nK, \qquad \alpha_0 = k_0\sqrt{\varepsilon^{(+1)}\mu}\,\sin\theta_0, \qquad K = 2\pi/p, \tag{6}$$

$$\beta_n^{(\pm 1)\pm} = \alpha_n\sin\zeta \pm [k_0^2\varepsilon^{(\pm 1)}\mu - \alpha_n^2]^{1/2}\cos\zeta, \times \mathrm{Re}\{[k_0^2\varepsilon^{(\pm 1)}\mu - \alpha_n^2]^{1/2}\} + \mathrm{Im}\{[k_0^2\varepsilon^{(\pm 1)}\mu - \alpha_n^2]^{1/2}\} > 0. \tag{7}$$

We denote by $U_\pm$ the sets of integers for which the β coefficients in Eq. (7) are real. Obviously, U_+ and U_- are the sets of the propagating diffraction orders in media $+1$ and -1.

Let $\eta_n{}^r$, $n \in U_+$, and $\eta_m{}^t$, $m \in U_-$, be the diffraction efficiencies in media $+1$ and -1, respectively. Then, for the reflected orders,

$$\eta_n^r = -\frac{\beta_n^{(+1)+} - \alpha_n\sin\zeta}{\beta_0^{(+1)-} - \alpha_0\sin\zeta}\,|R_n|^2, \qquad n \in U_+, \tag{8}$$

and for the transmitted orders,

$$\eta_n^t = \frac{\beta_n^{(-1)-} - \alpha_n\sin\zeta}{\beta_0^{(+1)-} - \alpha_0\sin\zeta}\,|T_n|^2, \qquad n \in U_-, \tag{9a}$$

$$\eta_n^t = \frac{\varepsilon^{(+1)}}{\varepsilon^{(-1)}}\,\frac{\beta_n^{(-1)-} - \alpha_n\sin\zeta}{\beta_0^{(+1)-} - \alpha_0\sin\zeta}\,|T_n|^2, \qquad n \in U_-. \tag{9b}$$

The diffraction angles are

$$\theta_n^{(\pm 1)} = \arcsin\frac{\alpha_n}{k_0\sqrt{\varepsilon^{(\pm 1)}\mu}}, \qquad n \in U_\pm. \tag{10}$$

To solve Eqs. (3) in region 0, we expand the field components into Floquet–Fourier series and expand the permittivity function ε and its inverse $a \equiv 1/\varepsilon$ into Fourier series:

$$F_l(x_1, x_2) = \sum_n F_{ln}(x_2)\exp(i\alpha_n x_1), \tag{11}$$

$$\varepsilon(x_1) = \sum_n \varepsilon_n \exp(inKx_1),$$

$$a(x_1) = \sum_n a_n \exp(inKx_1), \tag{12}$$

where F stands for E or H and $l = 1, 3$. Substituting Eqs. (11) and (12) into Eqs. (3) and assuming an x_2 dependence $F_{ln} \propto \exp(i\rho x_2)$, we get

$$\begin{bmatrix}\alpha\sin\zeta & k_0\mu\cos\zeta\\ \dfrac{\cos\zeta}{k_0\mu}\,(k_0^2[\![\varepsilon]\!]\mu - \alpha^2) & \alpha\sin\zeta\end{bmatrix}\begin{pmatrix}E_3\\H_1\end{pmatrix} = \rho\begin{pmatrix}E_3\\H_1\end{pmatrix}, \tag{13a}$$

$$\begin{bmatrix}\alpha\sin\zeta & -k_0[\![\varepsilon]\!]\cos\zeta\\ -\dfrac{\cos\zeta}{k_0}\,(k_0^2\mu - \alpha[\![a]\!]\alpha) & \alpha\sin\zeta\end{bmatrix}\begin{pmatrix}H_3\\E_1\end{pmatrix} = \rho\begin{pmatrix}H_3\\E_1\end{pmatrix}. \tag{13b}$$

In Eqs. (13), α is a diagonal matrix with elements α_n, $n = \ldots, -1, 0, +1, \ldots$, $[\![\varepsilon]\!]$ is a matrix such that $[\![\varepsilon]\!]_{mn} = \varepsilon_{m-n}$, $[\![a]\!]$ is defined similarly, and E_3, H_1, etc. should be understood as column vectors with elements E_{3n} and H_{1n}. Equations (13) are the matrix eigenvalue problem that we will solve.

To obtain the numerical solutions we truncate all Floquet–Fourier series to N terms, from $-(N-1)/2$ to $+(N-1)/2$, where N is an odd integer and will be called the truncation order. The Fourier series for ε and α should be truncated too, from $-(N-1)$ to $+(N-1)$, so the matrices that they form are $N \times N$. One can find the numerical solutions of Eq. (14a) and (14b) by calling an eigenproblem solver in a standard

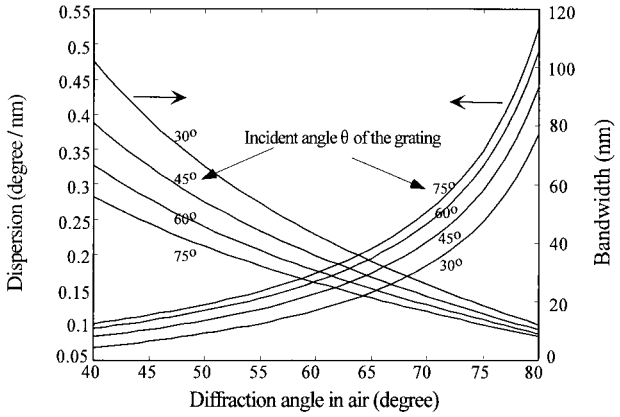

Fig. 3. Dispersion and approximate bandwidth of planar volume holographic gratings at a center wavelength of 1555 nm.

mathematical library. Each equation has $2N$ eigenvalues and the associated eigenvectors. The eigensolutions should be partitioned and sorted into two equal-dimensional sets.[7] We label the eigenvalues and eigenvectors by superscripts $\pm$ and index them by subscript q, $q = 1, 2, \ldots, N$.

Using the solutions of Eqs. (14), we find the total fields in region 0 in the form

$$\begin{bmatrix} E_3(x_1, x_2) \\ H_1(x_1, x_2) \end{bmatrix} = \sum_{n,q} \exp(i\alpha_n x_1) \left[\begin{pmatrix} E_{3nq}^{+} \\ H_{1nq}^{+} \end{pmatrix} \exp(i\rho_q^{+} x_2) C_q^{+} + \begin{pmatrix} E_{3nq}^{-} \\ H_{1nq}^{-} \end{pmatrix} \exp(i\rho_q^{-} x_2) C_q^{-} \right] \tag{14}$$

for TE polarization, with a similar equation for TM polarization. E_{3nq}, H_{1nq}, etc. are the elements of the eigenvector associated with the eigenvalue $\rho_q^{\pm}$, and $C_q^{\pm}$ are the unknown modal field amplitudes in region 0.

Matching the boundary conditions along the interfaces between regions ± 1 and region 0 leads to a large system of linear equations. The final solution for the unknown field amplitudes R_n and T_n are given by[7]

$$R_n = (S_{12})_{n0}, \qquad T_n = (S_{22})_{n0}, \tag{15}$$

where subscript $n0$ means the location of the matrix element at row n and column 0 and S_{12} and S_{22} can easily be derived from the S-matrix algorithm in Ref. 7.

3. Simulation Results of Holographic Gratings for WDDM Applications

For a path-reversed guided-wave transmission volume holographic grating used for WDDM there is a trade-off between the dispersion and the bandwidth.[3] Figure 3 plots grating dispersion and bandwidth as a function of diffraction angle at incident angles of 30°, 45°, 60°, and 75° at a center wavelength of 1555 nm. Simulation results of dispersion and bandwidth at a center wavelength of 800 nm can be found in Ref. 3. The thickness of the guided-wave holographic gratings is 20 μm. The refractive indices are $n_1 = [\varepsilon^{(+1)}]^{1/2} = 1.52$, $n_3 = [\varepsilon^{(-1)}]^{1/2} = 1.0$, and $n = [\varepsilon_0]^{1/2} = 1.52$. We select a 60° (incident angle of the grating)/60° (diffraction angle of the grating in air) grating structure for demultiplexing optical signals in the spectral region near 1555 nm and a 45°/45° structure for the spectral region near 800 nm. These structures provide reasonably large dispersion and acceptable bandwidth.

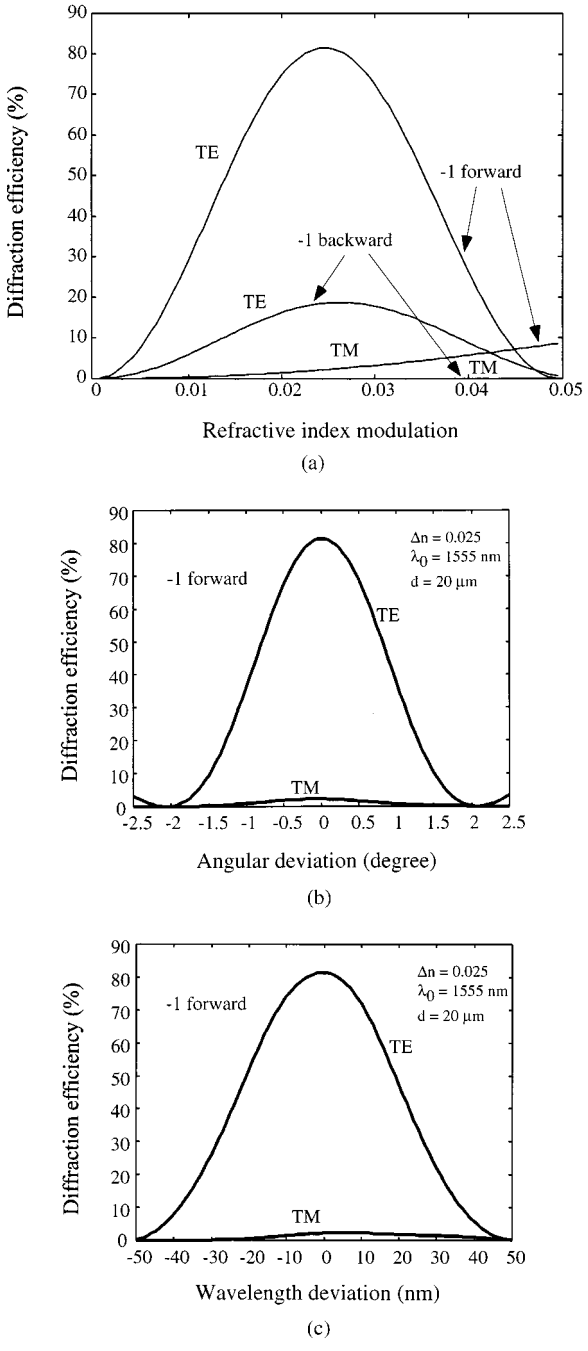

Fig. 4. RCWA simulation results for a 60°/60° grating structure at a center wavelength of 1555 nm.

The periodic permittivity $\varepsilon(X)$ of the grating is assumed to have a sinusoidal variation:

$$\varepsilon(X) = \varepsilon_0 + \varepsilon_1 \cos\left(\frac{2\pi X}{\Lambda}\right). \tag{16}$$

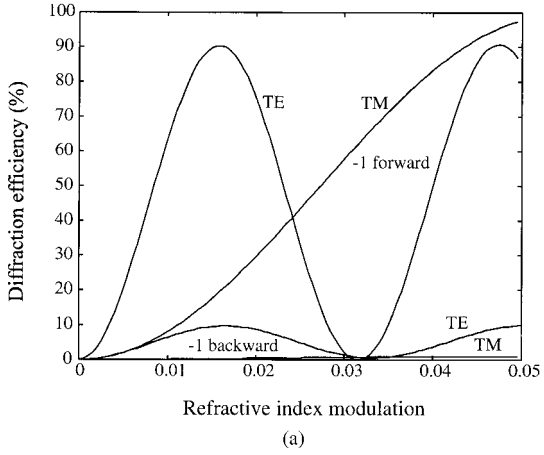

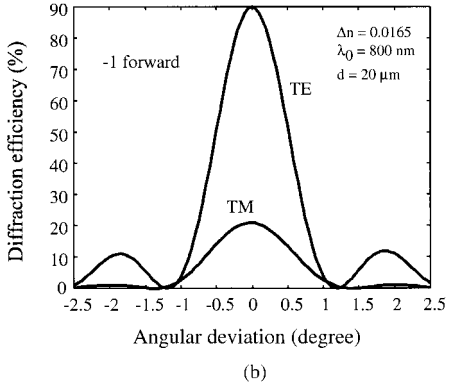

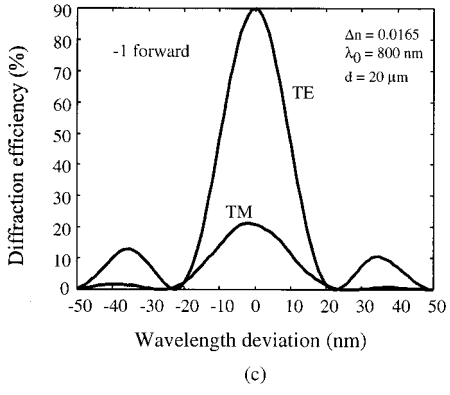

Fig. 5. RCWA simulation results for a 45°/45° grating structure at a center wavelength of 800 nm.

Using the method that we developed in Section 2, we simulated diffraction efficiency as a function of refractive-index modulation and angular and wavelength deviations for the selected gratings working at center wavelengths of 800 and 1555 nm. DuPont photopolymer film with a thickness of 20 μm was used in our simulation. There are one forward and one backward diffraction order for these two grating structures.[3] Figure 4 gives the simulation results of diffraction efficiencies versus refractive-index modulation [Fig. 4(a), angular deviation [Fig. 4(b)], and wavelength [Fig. 4(c)] for the 60°/60° grating structure working at a center wavelength of 1555 nm. It is shown that, within the dynamic range of the

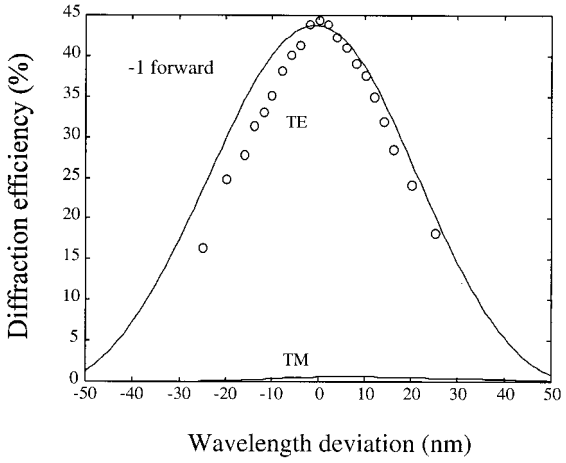

Fig. 6. Measured diffraction efficiency as a function of wavelength shift from 1555 nm. The RCWA simulation result is given at $\Delta n = 0.0128$.

refractive-index modulation of the DuPont photopolymer,[8,9] this structure is polarization sensitive. The 3-dB angular tolerance is 1.9°, and the 3-dB spectral bandwidth is 48 nm. The 1-dB bandwidth of 30 nm is matched with that of an erbium-doped fiber amplifier.[10] Figure 5 gives the simulation results for the 45°/45° structure working at 800 nm. The 3-dB angular tolerance is 1.2°, and the 3-dB spectral bandwidth is 21 nm.

4. Experimental Results at 800 and 1555 nm

We used a 532-nm Coherent Verdi laser to record the output holographic grating. A Ti:sapphire tunable laser was employed to characterize the performance of the device working at 800 nm, and an E-TEK tunable laser diode source for the device working at 1555 nm. DuPont photopolymer film HRF 600×001-20 with a thickness of 20 μm was chosen to record the guided-wave holographic gratings. The waveguiding plate had a thickness of 6.3 mm. The beveled angle α was 22.5° for the 45°/45° structure at 800 nm and 30° for the 60°/60° structure at 1555 nm.

Figure 6 gives the measured diffraction efficiencies of the −1-order forward diffraction as a function of wavelength deviation from a center wavelength of 1555 nm under a TE wave for the 60°/60° grating structure. The 3-dB bandwidth of this device was de-

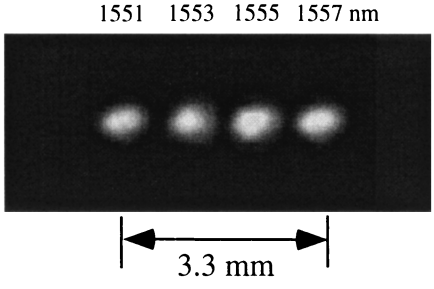

Fig. 7. CCD image taken at a focal plane of a focusing lens with a 20-cm focal length.

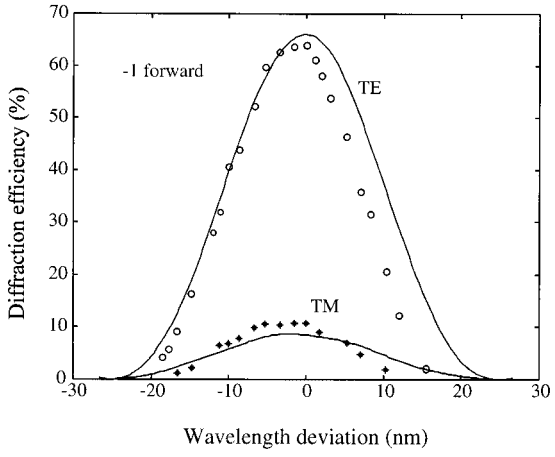

Fig. 8. Measured diffraction efficiency as a function of wavelength shift from 800 nm. The RCWA simulation result is given at $\Delta n = 0.012$.

termined to be 43 nm, which is close to that given in Section 3 and Fig. 6. Theoretical expectations (solid curve) are consistent with these experimental results (circles). The refractive-index modulation used for simulation was $\Delta n = 0.0128$. The measured dispersion of the grating (0.16°/nm) was polarization insensitive and consistent with the theoretical result.

Figure 7 is an experimental result of a four-channel WDDM operating at 1551, 1553, 1555, and 1557 nm, for which the bandwidth of the device can accommodate all four channels, as shown in Fig. 6, while maintaining a 2-nm wavelength separation. This image was taken with a CCD camera from the focal plane of a lens with a focal length of 20 cm. From Fig. 7 we can see that the four channels are totally separated and kept in good mode quality. With an aspheric lens it is possible to bring the light beams to a much smaller and to couple them into standard fiber bundles–arrays.

Similar results were obtained for the 45°/45° grating structure working at 800 nm.[3] A comparison between theory (solid curves) and experiment (circles and squares) is given in Fig. 8. The refractive-index modulation used for simulation was $\Delta n = 0.012$.

5. Summary

Path-reversed substrate-guided-wave holographic gratings were presented for WDDM applications. An efficient and practical method was developed to model the slanted volume holographic gratings. The dispersion and the bandwidth of the guided-wave holograms were analyzed. It was shown that by adjusting the incident angle and the diffraction angle of the path-reversed structure one can enhance the dispersion. Incident angles larger than the critical angle of the substrate can be obtained by beveling one edge of the waveguiding plate.

In our experiment we chose DuPont photopolymer film HRF 600×001-20 (20 μm thick) to record the holographic grating at center wavelengths of 800 and 1555 nm. A 60° (incident angle of the grating)/60° (diffraction angle of the grating in air) grating structure was employed to demultiplex optical signals in the 1555-nm spectral region; a 45°/45° grating structure, for the 800-nm spectral region. These structures provide large dispersion and acceptable bandwidth. The measured diffraction efficiencies are consistent with the theoretical results by RCWA. A four-channel WDDM separating wavelengths of 1551, 1553, 1555, and 1557 nm has been demonstrated. The bulky waveguiding glass plate provides mechanical and environmental robustness. As the dispersion occurs for the output holographic grating, the TEM_{00} mode profile of the dispersed optical signals with different optical wavelengths is well retained, and this also reduces the difficulties in integration with fiber arrays–bundles. This structure is expected to be cost effective and easy to fabricate compared with others, which are given as references in Ref. 3 and 11. This structure shows promise for use for dense wavelength-division multiplexing with channel spacing as small as 0.8 nm (100 GHz).

This research is supported by the Ballistic Missile Defense Organization, the U.S. Army Space and Strategic Defense Command, the Center of Optoelectronics Science and Technology, the Defense Advanced Research Projects Agency, the U.S. Office of Naval Research, the U.S. Air Force Office of Scientific Research, E. I. Dupont de Nemours and Company, Cray Research, Lightpath, the 3M Foundation, and the Advanced Technology Program of the state of Texas.

References

1. M. M. Li and R. T. Chen, "Five-channel surface-normal wavelength-division demultiplexer using substrate-guided waves in conjunction with a polymer-based Littrow hologram," Opt. Lett. **20,** 797–799 (1995).
2. Y. K. Tsai, Y. T. Huang, and D. C. Su, "Multiband wavelength-division demultiplexing with a cascaded substrate-mode grating structure," Appl. Opt. **34,** 5582–5588 (1995).
3. J. Liu and R. T. Chen, "Path-reversed photopolymer-based substrate-guided-wave optical interconnects for wavelength division demultiplexing," Appl. Opt. **38,** 3046–3052 (1999).
4. T. K. Gaylord and M. G. Moharam, "Analysis and applications of optical diffraction by gratings," Proc. IEEE **73,** 894–937 (1985).
5. D. M. Pai and K. A. Awada, "Analysis of dielectric gratings of arbitrary profiles and thickness," J. Opt. Soc. Am. A **8,** 755–762 (1991).
6. N. Chateau and J. P. Hugonin, "Algorithm for the rigorous coupled-wave analysis of grating diffraction," J. Opt. Soc. Am. A **11,** 1321–1331 (1991).
7. L. Li, "Formulation and comparison of two recursive matrix algorithms for modeling layered diffraction gratings," J. Opt. Soc. Am. A **11,** 1024–1035 (1996).
8. W. Gambogi, K. Steijn, S. Mackara, T. Duzik, B. Hamzavy, and J. Kelly, "HOE imaging in DuPont holographic photopolymers," in *Diffractive and Holographic Optics Technology*, I. Cindrich and S. H. Lee, eds., Proc. SPIE **2152,** 282–293 (1994).
9. U. Rhee, H. J. Caulfield, C. S. Vikram, and J. Shamir, "Dynamics of hologram recording in DuPont photopolymer," Appl. Opt. **34,** 846–853 (1995).
10. I. P. Kaminow and T. L. Koch, *Optical Fiber Telecommunications* (Academic, New York, 1997), Vol. IIIA.
11. J. Liu, "Multi-wavelength planar optoelectronic interconnections," Ph.D. dissertation (University of Texas at Austin, Austin, Tex., 1999).